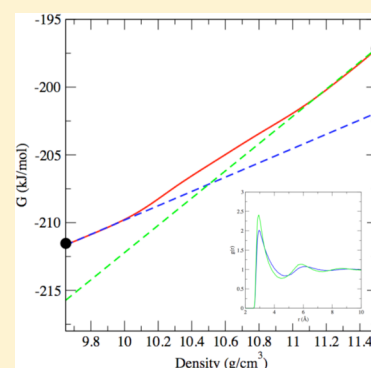


Thermodynamics of Phase Coexistence and Metal–Nonmetal Transition in Mercury: Assessment of Effective Potentials via Expanded Wang–Landau Simulations

Caroline Desgranges and Jerome Delhommelle*

Department of Chemistry, University of North Dakota, Grand Forks, North Dakota 58202, United States

ABSTRACT: We present molecular simulation results on the thermodynamics of phase transitions (specifically, the vapor–liquid and metal–nonmetal transitions) in mercury, as predicted by effective potential models. We use a recently developed method, known as Expanded Wang–Landau simulations, to determine the grand-canonical partition function of systems of mercury atoms. Using the statistical mechanics formalism, we are then able to determine all thermodynamic properties of the system, including the Gibbs free energy and entropy. Prior experimental and theoretical work has emphasized the strong interplay between the vapor–liquid coexistence and the metal–nonmetal transition. We therefore start by assessing the accuracy of the effective potentials considered in this work through a comparison to the available experimental data. We then analyze the thermodynamics of the nonmetal liquid–metal liquid transition, characterized by sharp variations in the rate of change of Gibbs free energy and enthalpy as a function of density. We also identify a crossover density (10.5 g/cm^3) consistent with the results of recent ab initio calculations and with the experiment.



INTRODUCTION

The development of new strategies to detect and remove mercury has been the focus of intense research in recent years.^{1–3} There are rising concerns about mercury as an industrial pollutant,⁴ since mercury emissions occur in industrial processes, from coal-fire power plants and during cement and mineral production.⁵ The toxicity of mercury and related forms is well documented^{6–8} and there is clearly a need for more efficient ways to remove this pollutant through, for example, its adsorption in novel sorbents.⁹ In conjunction with these experimental developments, there is also a need for accurate molecular models and simulation methods to better understand the behavior of mercury as well as its thermodynamics during these processes.

Mercury is a challenging system to model accurately^{10–14} and special care must be taken when considering an effective potential model for large-scale simulations of mercury. This is due to the unusual properties of this element.^{15,16} For instance, mercury has a very low melting point ($T_m = 234 \text{ K}$) when compared to the other 2B elements, that is, cadmium ($T_m = 594 \text{ K}$) and zinc ($T_m = 693 \text{ K}$).¹⁵ Similarly, the ratio between the melting temperature and the critical temperature is very low for mercury (0.13) and significantly below the ratio for cadmium (0.57) and zinc (0.59). Another challenging aspect that needs to be taken into account is the metal–nonmetal transition exhibited by mercury at high temperatures, known as the putative “Landau–Zeldovich first-order metal–nonmetal transition”.^{17–20}

Prior experimental and theoretical work has emphasized the strong interplay between the vapor–liquid coexistence and the metal–nonmetal transition.^{10,21} The first aim of this work is to

assess the ability of effective potentials to model the thermodynamic properties of mercury at the vapor–liquid coexistence. The second goal of this work is to characterize the thermodynamics of the metal–nonmetal transition, as modeled by effective models. We focus here on the thermodynamics of the transition, as a complete treatment of the electronic nature of this transition would require quantum methods. We will consider two types of effective potentials. Recent work has shown that including many-body interactions in the definition of effective potentials often results in very accurate results for many systems, ranging from rare gases^{22,23} to water^{24–26} and metals.^{27,28} The first type of effective potential model^{29,30} tested in this work is based on that strategy. It consists of a fit to an ab initio pair potential,³¹ supplemented with an effective many-body contribution. The second type of effective potential³² is based on a functional form that allows to recover the results obtained from an inversion of the experimental structure factor.^{33,34} We take advantage of the recently developed Expanded Wang–Landau (EWL) simulations^{35,36} to carry out a complete thermodynamic analysis using these effective potentials. The EWL method allows to calculate the partition function of the system and, from there, evaluate all thermodynamic properties of the system, including the Gibbs free energy and the entropy. The paper is organized as follows. We first present the effective potentials used to model the interactions between mercury atoms. We also discuss how we carry out EWL simulations to determine the partition function

Received: January 17, 2014

Revised: February 22, 2014

Published: February 25, 2014

of the system, and, in turn, the thermodynamic properties at the vapor–liquid coexistence. We then compare the predictions from the two effective potentials studied in this work to the available experimental data, including for the Gibbs free energy as well as for the entropy change associated with the vapor–liquid transition. We then extend our work to predict the variations of the thermodynamic properties of liquid mercury as a function of density and discuss the thermodynamics of the metal–nonmetal transition. We finally draw the main conclusions from this work in the last section.

EFFECTIVE POTENTIALS

The first effective potential we test is the Raabe-Sadus (RS) model.^{29,30} This potential can be described as the sum of an ab initio pair potential and of an effective multibody contribution. Mercury has been the topic of several ab initio studies,^{31,37–42} with recent work highlighting the importance of relativistic effects.^{31,37,39} The pair potential for Hg was fitted to the ab initio potential energy curve calculated at the coupled cluster level (CCSD(T)) and corrected for the basis set superposition error.³¹ A large uncontracted basis set (11s10p9d4f3g2h, noted as cc-ULB in ref 31, was used, together with energy-consistent scalar relativistic small-core pseudopotentials.^{43,44} Many-body effects were taken into account through an effective multibody contribution (C_9/r^9), with the parameter C_9 being fitted to reproduce the experimental liquid densities at a few selected temperatures below 1073 K.

The resulting potential is given by the following equation

$$\phi(r) = \lambda_E \sum_{j=3}^9 a_{2j} (\lambda_r r)^{-2j} - a_{SO} r^{-\alpha_{SO}} \exp(-\beta_{SO} r) + \frac{C_9}{r^9} \quad (1)$$

The parameters λ_E , λ_r , a_j , a_{SO} , α_{SO} , and β_{SO} (where the subscript SO denotes the spin–orbit correction) are given in ref 31. As discussed by Raabe and Sadus,²⁹ the ab initio pair potential exhibits a well depth of $\epsilon/k_B = 525.15$ K, with an excluded diameter of $\sigma = 3.14$ Å. Finally, the multibody effective parameter C_9 is temperature-dependent and is given by

$$C_9 = C_{9,0} + C_{9,1} \left(\frac{k_B T}{\epsilon} \right) \quad (2)$$

The values for the parameters $C_{9,0}$ and $C_{9,1}$ are given in ref 29.

The second effective potential considered in this work is the Bomont–Bretonnet (BB) model.³² It is based on a functional form proposed by Li et al.,⁴⁵ that allows to recover the general trends exhibited by potential obtained by inversion of the experimental structure factor³⁴ and the results of ab initio calculations using a quasirelativistic model potential with single and multireference singly and doubly excited configuration interactions (SRSDCI and MRSDCI) to account for electron correlations in both 5d and 6s electrons.⁴⁶ The functional form is as follows:

$$\phi(r) = A_0 \exp(-\alpha r) - A_1 \exp[-\beta(r - R_0)^2] \quad (3)$$

where the parameter A_1 is temperature-dependent^{32,47} and given by

$$A_1 = A_{1,0} + A_{1,1} T + A_{1,2} T^2 \quad (4)$$

Equation 4 applies only for temperatures below 1273 K and is constant (and equal to the value of A_1 at 1273 K) at higher temperatures. The values for the parameters A_0 , $A_{1,0}$, $A_{1,1}$, $A_{1,2}$,

α , β and R_0 are given in ref.³² The parameters of this model were fitted to reproduce the experimental densities for the liquid states along the vapor–liquid coexistence curve.

SIMULATION METHOD

We use the recently developed Expanded Wang–Landau simulations (EWL)^{35,36} to determine the thermodynamic properties of mercury over a wide range of conditions. We briefly outline the method here and refer the reader to our prior work^{35,36} for a detailed account of the method. This method consists in evaluating numerically the grand-canonical partition function of the system. Once the partition function is known, all thermodynamic properties of the system can be calculated through the statistical mechanics formalism. The EWL approach takes advantage of the Wang–Landau sampling scheme^{48–58} to evaluate dynamically the partition function. In addition, to ensure an accurate sampling of the grand-canonical ensemble, we implement an efficient scheme, based on the expanded ensemble approach,^{59–69} for the insertion of additional atoms into the system (as well as for the deletion of existing atoms). Since the insertion and deletion of entire atoms and molecules are often problematic, it has been suggested to divide the insertion, or deletion, in M stages, where M is an integer. At all times, the system is composed of N full atoms and of a fractional atom, which, for a given stage l ($0 \leq l \leq M - 1$), interacts with the full particles through a coupling parameter ξ_l . As discussed in prior work,^{35,36} this method allows us to evaluate numerically a simplified expanded grand-canonical partition function Θ_{SEGC} given by

$$\Theta_{\text{SEGC}}(\mu, V, T) = \sum_{N=0}^{\infty} \sum_{l=0}^{M-1} Q(N, V, T, l) \exp(\beta \mu N) \quad (5)$$

where $Q(N, V, T, l)$ is the canonical partition function for a system of N full atoms and a fractional atom. For a system with a void fractional particle ($l = 0$), $Q(N, V, T, 0)$ is the regular canonical partition function for a system of N atoms. For a system with a fractional atom at stage $l > 0$, $Q(N, V, T, l)$ is given by

$$Q(N, V, T, l) = \frac{V^{N+1}}{N! \Lambda^{3(N+1)}} \int \exp(-\beta U(\Gamma)) d\Gamma \quad (6)$$

In the expression above, the fractional atom is taken to have the same mass as a full atom, leading to the fact that they both have the same de Broglie wavelength Λ . Keeping only the results obtained for systems containing N full atoms and a void fractional atom (i.e., $l = 0$), we obtain the grand-canonical partition function of a system of mercury atoms as

$$\Theta(\mu, V, T) = \sum_{N=0}^{\infty} Q(N, V, T, l=0) \exp(\beta \mu N) \quad (7)$$

From a practical standpoint, EWL simulations are carried out within the framework of Monte Carlo (MC) simulations. To sample the configurations of the system, we perform MC steps corresponding to the translation of a single atom (75% of the MC steps) or to a change in (N, l) for the system (25% of the MC steps). The technical details regarding the Wang–Landau scheme are exactly the same as previously described,^{35,36} with the final value of the convergence factor set to $f = 10^{-8}$ and a number of intermediate stages set to $M = 100$. Expanded Wang–Landau were run on systems containing up to a total of

500 atoms. Finally, we use a spherical truncation for the calculation of interatomic interactions, with the usual tail corrections applied beyond the cutoff set to half the boxlength.⁷⁰

RESULTS AND DISCUSSION

We first present the results obtained for the partition functions with the RS and the BB model in Figure 1a. The canonical

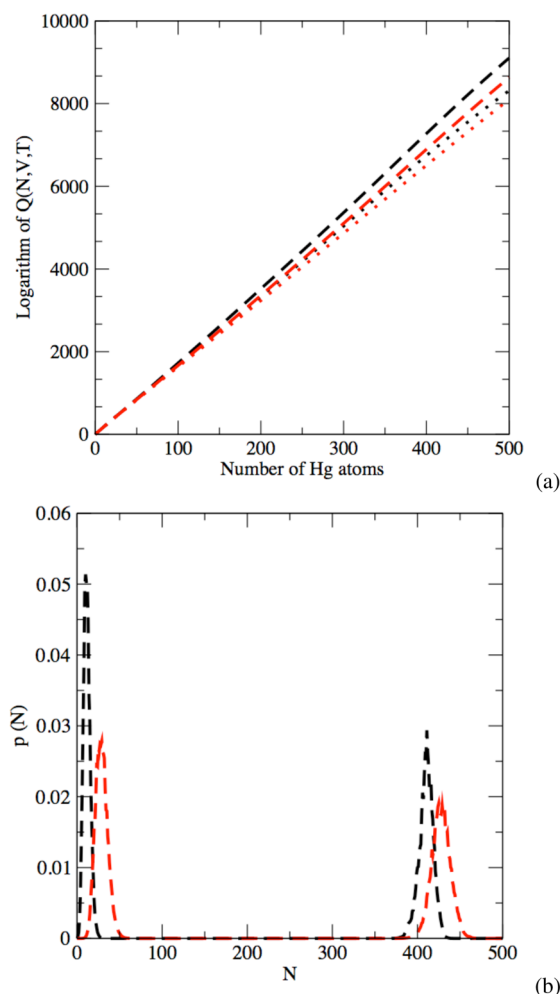


Figure 1. (a) Comparison of the logarithm of the canonical partition function $Q(N, V, T)$ obtained with the RS model (in red) and with the BB model (in black). Results are shown for two different temperatures: $T = 1073$ K (dashed line) and at $T = 1473$ K (dotted line). (b) Distribution number $p(N)$ for $T = 1373$ K at the vapor–liquid coexistence: RS model (red) and BB model (black).

partition functions obtained during the EWL simulations are key quantities, since they allow for the calculation of the grand-canonical partition function and the determination of all the thermodynamic properties of the system through the formalism of statistical mechanics. Figure 1a shows a comparison between the canonical partition functions of the two models at $T = 1073$ K and $T = 1473$ K. This plot emphasizes the direct impact of the choice of a specific force field on the partition function. We estimate from Figure 1a the deviation between the RS partition function and the BB partition function to be of the order of 5.5% at $T = 1473$ K and of 2.4% at $T = 1073$ K.

The next step consists in assessing the ability of the two models to predict the thermodynamic properties of mercury at

coexistence, and, in particular, the Gibbs free energy as well as the entropy change at the vapor–liquid transition. This step starts with the determination of the conditions of coexistence. From a statistical mechanics standpoint, this corresponds to the values of the chemical potential leading to equal probabilities for the vapor (Π_v) and for the liquid phase (Π_l). In practice, the probability for each phase is calculated using the number probability distribution $p(N)$, where N is the number of mercury atoms given by

$$p(N) = \frac{Q(N, V, T) \exp(\beta\mu N)}{\Theta(\mu, V, T)} \quad (8)$$

The chemical potential at coexistence is then obtained by writing the condition $\Pi_v = \Pi_l$ and numerically solving the corresponding equation

$$\begin{aligned} \sum_{N < N_b} \frac{Q(N, V, T) \exp(\beta\mu N)}{\Theta(\mu, V, T)} \\ = \sum_{N > N_b} \frac{Q(N, V, T) \exp(\beta\mu N)}{\Theta(\mu, V, T)} \end{aligned} \quad (9)$$

In eq 9, the left-hand side is the probability associated with the vapor Π_v and the right-hand side is the probability associated with the liquid Π_l (N_b is the value of N for which $p(N)$ reaches its minimum).

Figure 1b shows the number probability distribution at coexistence for the RS and BB models at $T = 1373$ K. This plot shows, for each model, the two peaks corresponding to the two coexisting phases, the vapor peak for low N values and the liquid peak for high N values. The different canonical partition functions obtained with the two models (as shown in Figure 1a) result in different chemical potentials at coexistence with a deviation of 4.5% at $T = 1373$ K ($\mu_{RS} = -191.26$ kJ/mol as compared to $\mu_{BB} = -199.91$ kJ/mol).

We plot in Figure 2 the variation of the Gibbs free energy at coexistence as a function of temperature for the RS and the BB model, together with the experimental data.⁷¹ Figure 2 shows that the results obtained with the RS model are in very good agreement with the experiment (within 1% for all temper-

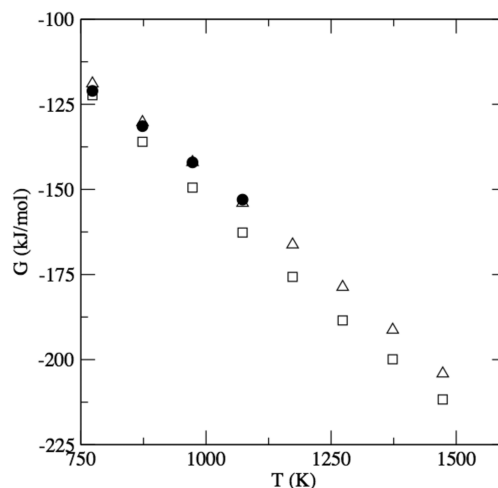


Figure 2. Gibbs free energy at the vapor–liquid coexistence: experimental data⁷¹ are shown as filled circles, EWL results using the RS model are shown as triangles and EWL results using the BB model are shown as squares.

atures), while the BB model underestimates the experimental data (by a maximum of 6% at the highest temperature for which data are available). At low temperatures, both models yield similar values, as well as an accurate prediction of the Gibbs free energy coexistence. As the temperature decreases, the density of the vapor at coexistence decreases, behaving more and more as an ideal gas. Therefore, at low temperatures, the Gibbs free energy at coexistence will essentially reflect how well the liquid phase is modeled by a given force field. The agreement observed here between the predictions of the two models and the experiment is consistent with the fact that the models were optimized by fitting some of the properties of the liquid phase (specifically, the variations of the density of the liquid as a function of temperature).

There is also another effect of the difference in the value of the partition function that can be seen in Figure 1b. We observe a slight shift of both peaks toward the lower values for N , when switching from the RS model to the BB model. This suggests that the difference observed between the RS and BB partition functions will result in a shift of the vapor–liquid coexistence curve of the BB model toward lower densities, with respect to the curve obtained for the RS model. To fully assess this point, we calculate the coexisting densities for the two models using the following relations:

$$\begin{aligned}\langle \rho_l \rangle &= \sum_{N > N_b} \frac{N}{V} p(n) \\ \langle \rho_v \rangle &= \sum_{N < N_b} \frac{N}{V} p(n)\end{aligned}\quad (10)$$

The resulting densities at coexistence are shown for the two models in Figure 3). The results presented in Figure 3 confirm

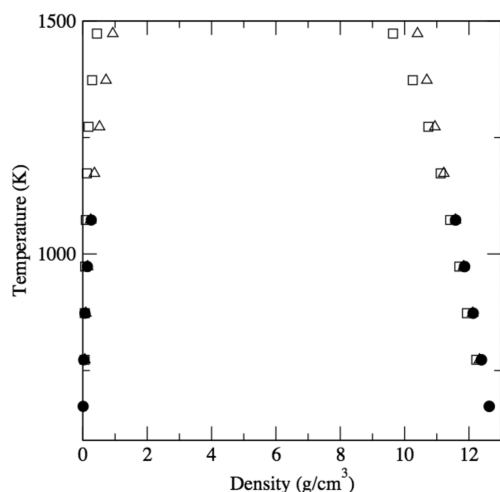


Figure 3. Vapor–liquid equilibria for mercury (same legend as Figure 2).

that the BB vapor–liquid equilibrium is shifted to the left (low densities) with respect to the RS vapor–liquid equilibrium. The agreement between the predictions from the two models is good at low temperatures (e.g., the liquid densities for the two models are within 1% of each other for temperatures up to 1173 K) and the shift in the coexistence curve only becomes significant at high temperatures. Figure 3 also provides a comparison with the experiment and show that the coexisting densities predicted by the two models are in very good

agreement with the experimental densities for temperatures up to 1073 K.

We now move on to the dependence of vapor pressure on temperature. For this purpose, we determine the vapor pressure from the EWL results by using the following equation:

$$P = \frac{k_B T \ln \Theta(\mu, V, T)}{V} \quad (11)$$

We plot in Figure 4 the results obtained for the two models and compare them to the data generated by using a correlation

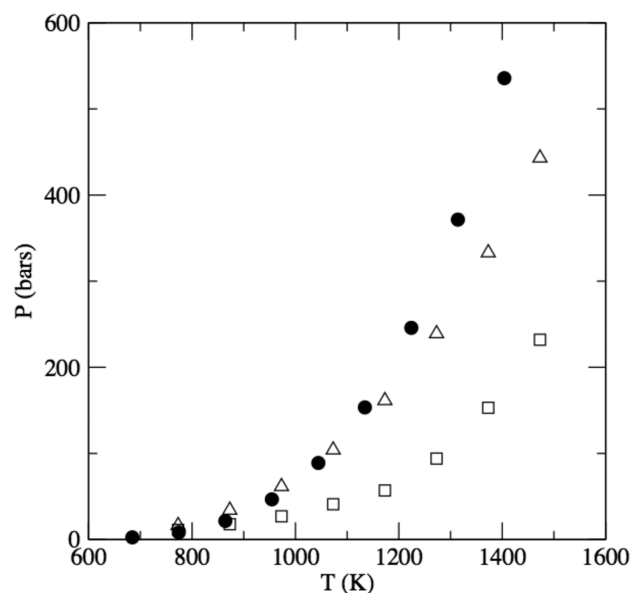


Figure 4. Vapor pressure: correlation data⁷² are shown as filled circles, EWL results using the RS model are shown as triangles and EWL results using the BB model are shown as squares.

equation.⁷² Again, the two models perform reasonably well at low temperatures, with the RS model overestimating slightly the correlation data and the BB model underestimating these data. However, at high temperature, the results show that the two models underestimate the vapor pressure data. While the RS model provides a good agreement with the experiment up to about 1200 K, the BB model starts to underestimate significantly the vapor pressure for temperatures greater than 1000 K. These results can be related to the much lower densities for the vapor phase predicted by the BB model at high temperatures.

We now examine the performance of the two models with respect to the prediction of the entropy of mercury. We start by determining the internal energy for the liquid U_{liq} and for the vapor U_{vap} at coexistence:

$$\begin{aligned}U_{liq} &= \frac{\sum_{N > N_b} (E_{pot}(N) + \frac{3}{2}k_B T) p(N)}{\sum_{N > N_b} p(N)} \\ U_{vap} &= \frac{\sum_{N < N_b} (E_{pot}(N) + \frac{3}{2}k_B T) p(N)}{\sum_{N < N_b} p(N)}\end{aligned}\quad (12)$$

in which $E_{pot}(N)$ is the average potential energy per mercury atom collected during the EWL simulation. The kinetic (ideal gas) contribution $(3/2)k_B T$ stems from the three degrees of freedom of translation per mercury atom. Once the internal

energies have been determined, we calculate the entropies for the two phases at coexistence according to

$$S_{\text{liq}} = \frac{k_B \ln \Theta(\mu, V, T)}{\langle N_{\text{liq}} \rangle} + \frac{(U_{\text{liq}} - \mu)}{T}$$

$$S_{\text{vap}} = \frac{k_B \ln \Theta(\mu, V, T)}{\langle N_{\text{vap}} \rangle} + \frac{(U_{\text{vap}} - \mu)}{T} \quad (13)$$

We plot in Figure 5 the entropy for the vapor and liquid phases, as well as the entropy change as a result of the vapor–

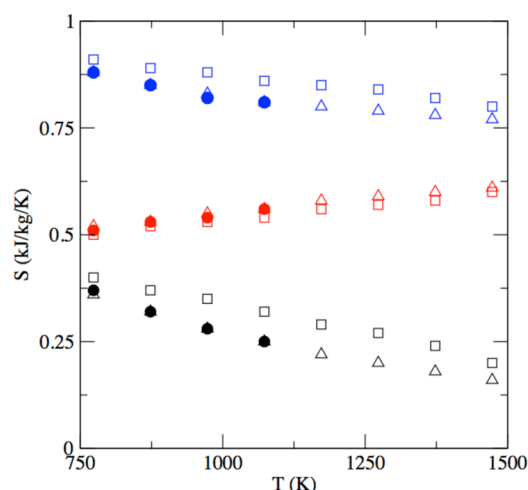


Figure 5. Entropy at coexistence for the liquid phase (shown in red), the vapor phase (shown in blue), and entropy change as a result of the transition (shown in black): experimental data⁷¹ are shown as filled circles, EWL results using the RS model are shown as triangles, and EWL results are shown as squares.

liquid transition. We start by commenting on the results obtained for the liquid phase. The RS and BB entropies for the liquid phase are in very good agreement with each other and with the experimental data (within 0.02 kJ/kg/K for all temperatures), reflecting that both RS and BB models perform well for the liquid phase. For the vapor, the BB entropy is found to overestimate the experimental data, with the deviation from the experiment becoming more important as the temperature increases (from 0.03 kJ/kg/K at 773 K up to 0.05 kJ/kg/K at 1073 K). This result is in line with our results on the vapor density and vapor pressure, which tend to indicate that the BB model underestimates the vapor density and as a result overestimate its entropy. On the other hand, the vapor entropies obtained using the RS model are in very good agreement with the experimental data (within 0.01 kJ/kg/K for all temperatures). As a result, we obtain a very good agreement with the experimental data for the entropy change associated with the transition in the RS model and only a good agreement in the case of the BB model.

We now turn to the thermodynamic characterization of the metal–nonmetal transition predicted by these effective models. As shown in prior work,³² the BB model exhibits a transition akin to the metal–nonmetal transition. This transition is associated with a nontrivial dependence of the number of nearest neighbors in the first coordination shell on the density.^{32,34,73} We therefore use the partition functions calculated during the EWL simulations to determine the evolution of the properties of the liquid as a function of density.

In the rest of the paper, we present results obtained with the BB model as we were unable to locate the metal–nonmetal transition in the results obtained with the RS model. We focus on the results obtained at $T = 1373$ K and plot in Figure 6 the

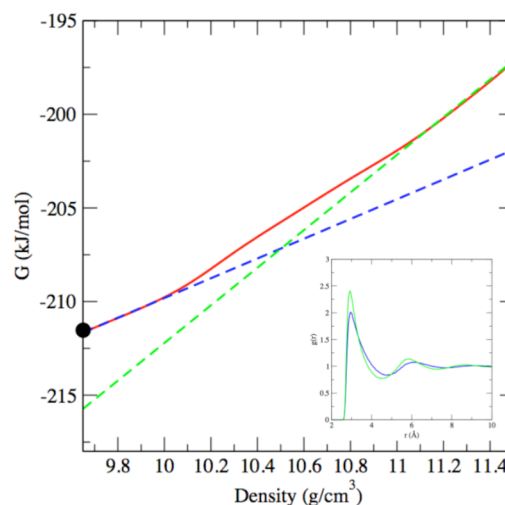


Figure 6. Gibbs free energy of the liquid phase for the BB model at $T = 1473$ K as a function of the density. EWL results are shown with a red solid line. The two linear fits indicate the limiting behavior at low density (in blue) and at high density (in green). The filled circles (for $d = 9.65$ g/cm³ and $d = 11.5$ g/cm³) on the free energy curve are two state points for which we show the pair correlation function $g(r)$ in the bottom right corner.

variations of the Gibbs free energy of the liquid as a function of density. This is obtained by calculating the density through the following equation for all chemical potentials:

$$\langle \rho \rangle = \sum_N \frac{N}{V} \frac{Q(N, V, T) \exp(\beta \mu N)}{\Theta(\mu, V, T)} \quad (14)$$

In eq 14, the chemical potential is taken to be greater than the chemical potential at coexistence, leading to a single peaked number probability distribution in the liquid region of the phase diagram. As a result, the sum in eq 14 is taken over all possible values for N .

Figure 6 shows a marked change in the variations of the Gibbs free energy G as a function of the density between the low density regime (below 10 g/cm³) and the high density regime (above 11 g/cm³). Throughout the density change, the system remains in the liquid phase as evidenced by the pair correlation functions shown in Figure 6. We also plot in Figure 6 linear fits to the EWL results for G in those two regimes. The two linear fits, which intersect at a density close to 10.5 g/cm³, clearly indicate a change in slope between the two regimes. The low density regime, corresponding to the nonmetal liquid, is associated with a slow increase of the Gibbs free energy with the density, while the high density regime, corresponding to the metal phase, is associated with a rapid increase in Gibbs free energy with the density. We add that the crossover point of 10.5 g/cm³ obtained in this work is consistent with the estimates from the experimental data^{74,75} and from ab initio calculations.²⁰

The next properties we examine are the enthalpy H and the entropy S of the liquid as a function of the density, as predicted by the BB model. The internal energy, enthalpy, and entropy of the liquid can be calculated from the EWL results as follows:

$$\begin{aligned}
 U &= \sum_N \left(E_{\text{pot}}(N) + \frac{3}{2} k_B T \right) p(N) \\
 H &= \frac{k_B T \ln \Theta(\mu, V, T)}{\langle N \rangle} + U \\
 S &= \frac{k_B \ln \Theta(\mu, V, T)}{\langle N \rangle} + \frac{(U - \mu)}{T}
 \end{aligned} \quad (15)$$

where, in line with our calculations for G , the chemical potential is taken to be greater than the chemical potential at coexistence and $\langle N \rangle$ indicates the average number of mercury atoms in the system.

We present in Figures 7 and 8 the results obtained for the enthalpy and the entropy, respectively. The enthalpy exhibits a

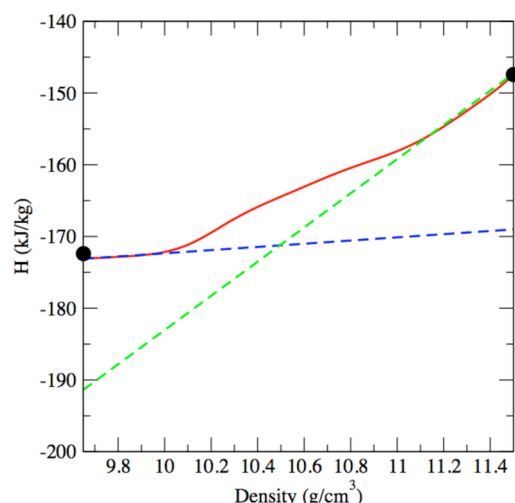


Figure 7. Enthalpy of the liquid phase for the BB model at $T = 1473$ K as a function of density (same legend as Figure 6).

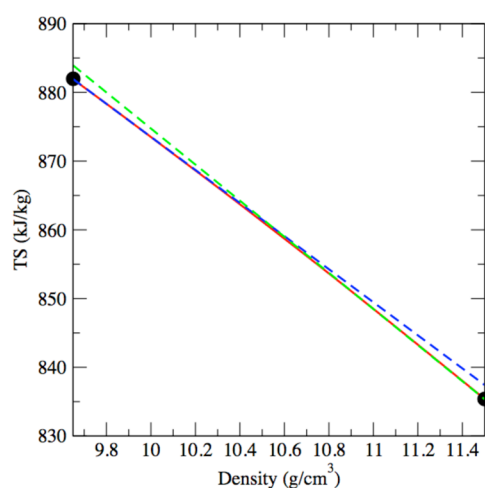


Figure 8. Entropy of the liquid phase for the BB model at $T = 1473$ K as a function of density (same legend as Figure 6).

very similar behavior to that observed for the Gibbs free energy. Again, we observe a notable change of behavior between the low density and high density regimes. In line with the results for the Gibbs free energy, the enthalpy is found to increase slowly with density in the low density regime and to increase at a much faster rate with density in the high density regime. This is

shown in Figure 7 by the linear fits to the two regimes, which once again intersects for a density close to 10.5 g/cm^3 . We then move on to the results for the entropy. As shown in Figure 8, the effect of the metal–nonmetal transition on entropy is much less pronounced. The results show a slight change in slope as the system moves from the low density regime to the high density regime, with the two linear fits crossing again for a density close to 10.5 g/cm^3 .

CONCLUSIONS

In this work, we used EWL simulations to provide a full picture of the thermodynamics of mercury at the vapor–liquid coexistence and at the metal–nonmetal transition using two effective potentials. The two effective potentials were based on the results of ab initio calculations, with effective parameters fitted to reproduce the variations of the density of the liquid along the vapor–liquid coexistence curve. Using the partition functions evaluated via EWL simulations and the statistical mechanics formalism, we were able to determine the properties of mercury at the vapor–liquid coexistence, including the Gibbs free energy and the entropies of the coexisting phases. The comparison with the experimental data show that the Gibbs free energy and the entropies at coexistence are correctly accounted for by both models. While the BB effective potential yielded a less satisfactory agreement with the correlation data for the vapor pressure, this model was able to account for the metal–nonmetal transition. Continuing our analysis of the EWL simulation results, we related the metal–nonmetal transition for the BB model to sharp changes in the rate of variations of the Gibbs free energy and of enthalpy as a function of density.

AUTHOR INFORMATION

Corresponding Author

*E-mail: jerome.delhommelle@und.edu. Phone: 701-777-2495.

Notes

The authors declare no competing financial interest.

ACKNOWLEDGMENTS

Partial funding for this research was provided by NSF through CAREER award DMR-1052808.

REFERENCES

- (1) Wu, C.; Cao, Y.; Dong, Z.; Cheng, C.; Li, H.; Pan, W. Evaluation of Mercury Speciation and Removal through Air Pollution Control Devices of a 190 MW Boiler. *J. Environ. Sci.* **2010**, *22*, 277–282.
- (2) Tao, S.; Li, C.; Fan, X.; Zeng, G.; Lu, P.; Zhang, X.; Wen, Q.; Zhao, W.; Luo, D.; Fan, C. Activated Coke Impregnated with Cerium Chloride Used for Elemental Mercury Removal from Simulated Flue Gas. *Chem. Eng. J.* **2012**, *210*, 547–556.
- (3) Hua, X.-Y.; Zhou, J.-S.; Li, Q.; Luo, Z.-Y.; Cen, K.-F. Gas-Phase Elemental Mercury Removal by CeO_2 Impregnated Activated Coke. *Energy Fuels* **2010**, *24*, 5426–5431.
- (4) Selin, N. E. Mercury Rising: Is Global Action Needed to Protect Human Health and the Environment? *Environ.: Sci. Policy Sustainable Dev.* **2005**, *47*, 22–35.
- (5) Zheng, Y.; Jensen, A. D.; Windelin, C.; Jensen, F. Review of Technologies for Mercury Removal from Flue Gas from Cement Production Processes. *Prog. Energy Combust. Sci.* **2012**, *38*, 599–629.
- (6) Carvalho, C. M.; Lu, J.; Zhang, X.; Arnér, E. S.; Holmgren, A. Effects of Selenite and Chelating Agents on Mammalian Thioredoxin Reductase Inhibited by Mercury: Implications for Treatment of Mercury Poisoning. *FASEB J.* **2011**, *25*, 370–381.

- (7) Clarkson, T. W. Human Toxicology of Mercury. *J. Trace Elem. Exp. Med.* **1998**, *11*, 303–317.
- (8) Zahir, F.; Rizwi, S. J.; Haq, S. K.; Khan, R. H. Low Dose Mercury Toxicity and Human Health. *Environ. Toxicol. Phar.* **2005**, *20*, 351–360.
- (9) Tan, Z.; Sun, L.; Xiang, J.; Zeng, H.; Liu, Z.; Hu, S.; Qiu, J. Gas-Phase Elemental Mercury Removal by Novel Carbon-Based Sorbents. *Carbon* **2012**, *50*, 362–371.
- (10) Hensel, F.; Warren, W. W. *Fluid Metals: The Liquid–Vapor Transition of Metals*; Princeton University Press: Princeton, NJ, 1999.
- (11) Paulus, B.; Rosciszewski, K.; Gaston, N.; Schwerdtfeger, P.; Stoll, H. Convergence of the Ab Initio Many-Body Expansion for the Cohesive Energy of Solid Mercury. *Phys. Rev. B* **2004**, *70*, 165106.
- (12) Gaston, N.; Schwerdtfeger, P. From the van der Waals Dimer to the Solid State of Mercury with Relativistic Ab Initio and Density Functional Theory. *Phys. Rev. B* **2006**, *74*, 024105.
- (13) Gaston, N.; Paulus, B.; Rosciszewski, K.; Schwerdtfeger, P.; Stoll, H. Lattice Structure of Mercury: Influence of Electronic Correlation. *Phys. Rev. B* **2006**, *74*, 094102.
- (14) Hermann, A.; Krawczyk, R. P.; Lein, M.; Schwerdtfeger, P.; Hamilton, I. P.; Stewart, J. J. Convergence of the Many-Body Expansion of Interaction Potentials: From van der Waals to Covalent and Metallic Systems. *Phys. Rev. A* **2007**, *76*, 013202.
- (15) Ashcroft, N. W.; Mermin, N. D. *Solid State Physics*; Brooks/Cole, Thomson Learning: Stamford, CT, 1976.
- (16) Chacón, E.; Reinaldo-Falagan, M.; Velasco, E.; Tarazona, P. Layering at Free Liquid Surfaces. *Phys. Rev. Lett.* **2001**, *87*, 166101.
- (17) Landau, L.; Zeldovich, Y. B. On the Relation between the Liquid and the Gaseous States of Metals. *Acta Physicochim. USSR* **1943**, *18*, 194.
- (18) Schonherr, G.; Schmutzler, R.; Hensel, F. Electrical and Thermodynamic Properties of Mercury in the Metal–Semiconductor Transition Range. *Philos. Mag. B* **1979**, *40*, 411–423.
- (19) Kresse, G.; Hafner, J. Ab Initio Simulation of the Metal/Nonmetal Transition in Expanded Fluid Mercury. *Phys. Rev. B* **1997**, *55*, 7539–7548.
- (20) Calderín, L.; González, L.; González, D. Static, Dynamic and Electronic Properties of Expanded Fluid Mercury in the Metal–Nonmetal Transition Range. An Ab Initio Study. *J. Phys.: Condens. Matter* **2011**, *23*, 375105.
- (21) Korobenko, V.; Rakhel, A. Direct Measurements of Thermodynamic Functions and Electrical Resistivity of Fluid Tungsten over a Wide Range of Densities. *Phys. Rev. B* **2013**, *88*, 134203.
- (22) Nasrabad, A. E.; Laghaei, R.; Deiters, U. Prediction of the Thermophysical Properties of Pure Neon, Pure Argon, and the Binary Mixtures Neon–Argon and Argon–Krypton by Monte Carlo Simulation Using Ab Initio Potentials. *J. Chem. Phys.* **2004**, *121*, 6423–6434.
- (23) Marcelli, G.; Sadus, R. J. Molecular Simulation of the Phase Behavior of Noble Gases Using Accurate Two-Body and Three-Body Intermolecular Potentials. *J. Chem. Phys.* **1999**, *111*, 1533–1540.
- (24) Hermann, A.; Schwerdtfeger, P. Ground-State Properties of Crystalline Ice from Periodic Hartree-Fock Calculations and a Coupled-Cluster-Based Many-Body Decomposition of the Correlation Energy. *Phys. Rev. Lett.* **2008**, *101*, 183005.
- (25) Tainter, C.; Pieniazek, P.; Lin, Y.-S.; Skinner, J. Robust Three-Body Water Simulation Model. *J. Chem. Phys.* **2011**, *134*, 184501.
- (26) Babin, V.; Medders, G. R.; Paesani, F. Toward a Universal Water Model: First Principles Simulations from the Dimer to the Liquid Phase. *J. Phys. Chem. Lett.* **2012**, *3*, 3765–3769.
- (27) Luo, S.-N.; Ahrens, T. J.; Çağrı, T.; Strachan, A.; Goddard, W. A., III; Swift, D. C. Maximum Superheating and Undercooling: Systematics, Molecular Dynamics Simulations, and Dynamic Experiments. *Phys. Rev. B* **2003**, *68*, 134206.
- (28) Aleksandrov, T.; Desgranges, C.; Delhommelle, J. Vapor–Liquid Equilibria of Copper Using Hybrid Monte Carlo Wang–Landau Simulations. *Fluid Phase Equilib.* **2010**, *287*, 79–83.
- (29) Raabe, G.; Sadus, R. J. Molecular Simulation of the Vapor–Liquid Coexistence of Mercury. *J. Chem. Phys.* **2003**, *119*, 6691–6697.
- (30) Raabe, G.; Todd, B.; Sadus, R. J. Molecular Simulation of the Shear Viscosity and the Self-Diffusion Coefficient of Mercury along the Vapor–Liquid Coexistence Curve. *J. Chem. Phys.* **2005**, *123*, 034511.
- (31) Schwerdtfeger, P.; Wesendrup, R.; Moyano, G. E.; Sadlej, A. J.; Greif, J.; Hensel, F. The Potential Energy Curve and Dipole Polarizability Tensor of Mercury Dimer. *J. Chem. Phys.* **2001**, *115*, 7401–7412.
- (32) Bomont, J.-M.; Bretonnet, J.-L. An Effective Pair Potential for Thermodynamic and Structural Properties of Liquid Mercury. *J. Chem. Phys.* **2006**, *124*, 054504.
- (33) Munejiri, S.; Shimojo, F.; Hoshino, K. The Density Dependence of the Velocity of Sound in Expanded Liquid Mercury studied by Means of a Large-Scale Molecular-Dynamics Simulation. *J. Phys.: Condens. Matter* **1998**, *10*, 4963–4974.
- (34) Toth, G. An Iterative Scheme to Derive Pair Potentials from Structure Factors and Its Application to Liquid Mercury. *J. Chem. Phys.* **2003**, *118*, 3949–3955.
- (35) Desgranges, C.; Delhommelle, J. Evaluation of the Grand-Canonical Partition Function using Expanded Wang–Landau Simulations. I. Thermodynamic Properties in the Bulk and at the Liquid–Vapor Phase Boundary. *J. Chem. Phys.* **2012**, *136*, 184107.
- (36) Desgranges, C.; Delhommelle, J. Evaluation of the Grand-Canonical Partition Function using Expanded Wang–Landau Simulations. II. Adsorption of Atomic and Molecular Fluids in a Porous Material. *J. Chem. Phys.* **2012**, *136*, 184108.
- (37) Munro, L. J.; Johnson, J. K.; Jordan, K. D. An Interatomic Potential for Mercury Dimer. *J. Chem. Phys.* **2001**, *114*, 5545–5551.
- (38) Gaston, N.; Schwerdtfeger, P.; Saue, T.; Greif, J. The Frequency-Dependent Dipole Polarizability of the Mercury Dimer from Four-Component Relativistic Density-Functional Theory. *J. Chem. Phys.* **2006**, *124*, 044304.
- (39) Calvo, F.; Pahl, E.; Wormit, M.; Schwerdtfeger, P. Evidence for Low-Temperature Melting of Mercury owing to Relativity. *Angew. Chem., Int. Ed.* **2013**, *52*, 7583–7585.
- (40) Kitamura, H. The Role of Attractive Many-Body Interaction in the Gas–Liquid Transition of Mercury. *J. Phys.: Condens. Matter* **2007**, *19*, 072102.
- (41) Kitamura, H. Equation of State for Expanded Fluid Mercury: Variational Theory with Many-Body Interaction. *J. Chem. Phys.* **2007**, *126*, 134509.
- (42) Bučinský, L.; Biskupič, S.; Ilčin, M.; Lukeš, V.; Laurinc, V. Relativistic Effects in HgHe and HgXe CCSD (T) Ground State Potential Curves. Low-Density Viscosity Simulations of Hg:Xe Mixture. *J. Comput. Chem.* **2011**, *32*, 356–367.
- (43) Küchle, W.; Dolg, M.; Stoll, H.; Preuss, H. Ab Initio Pseudopotentials for Hg through Rn: I. Parameter Sets and Atomic Calculations. *Mol. Phys.* **1991**, *74*, 1245–1263.
- (44) Häussermann, U.; Dolg, M.; Stoll, H.; Preuss, H.; Schwerdtfeger, P.; Pitzer, R. Accuracy of Energy-Adjusted Quasirelativistic Ab Initio Pseudopotentials: All-Electron and Pseudopotential Benchmark Calculations for Hg, HgH and Their Cations. *Mol. Phys.* **1993**, *78*, 1211–1224.
- (45) Li, Y.; Blaisten-Barojas, E.; Papaconstantopoulos, D. Structure and Dynamics of Alkali-Metal Clusters and Fission of Highly Charged Clusters. *Phys. Rev. B* **1998**, *57*, 15519–15532.
- (46) Sumi, T.; Miyoshi, E.; Sakai, Y.; Matsuoka, O. Molecular-Orbital and Molecular-Dynamics Study of Mercury. *Phys. Rev. B* **1998**, *57*, 914–918.
- (47) Bomont, J.-M.; Delhommelle, J.; Bretonnet, J.-L. Structure and Thermodynamics of the Expanded Liquid Mercury by Monte Carlo Simulation: A First Attempt. *J. Non-Cryst. Solids* **2007**, *353*, 3454–3458.
- (48) Wang, F.; Landau, D. P. Determining the Density of States for Classical Statistical Models: A Random Walk Algorithm To Produce a Flat Histogram. *Phys. Rev. E* **2001**, *64*, 056101.
- (49) Wang, F.; Landau, D. Efficient, Multiple-Range Random Walk Algorithm to calculate the Density of States. *Phys. Rev. Lett.* **2001**, *86*, 2050–2053.

- (50) Shell, M. S.; Debenedetti, P. G.; Panagiotopoulos, A. Z. Generalization of the Wang–Landau Method for Off-Lattice Simulations. *Phys. Rev. E* **2002**, *66*, 056703.
- (51) Yan, Q.; Faller, R.; de Pablo, J. J. Density-of-States Monte Carlo Method for Simulation of Fluids. *J. Chem. Phys.* **2002**, *116*, 8745–8750.
- (52) Gazenmüller, G.; Camp, P. J. Applications of Wang–Landau Sampling to Determine Phase Equilibria in Complex Fluids. *J. Chem. Phys.* **2007**, *127*, 154504.
- (53) Desgranges, C.; Delhommelle, J. Phase Equilibria of Molecular Fluids via Hybrid Monte Carlo Wang–Landau Simulations: Applications to Benzene and *n*-Alkanes. *J. Chem. Phys.* **2009**, *130*, 244109.
- (54) Desgranges, C.; Kastl, E. A.; Aleksandrov, T.; Delhommelle, J. Optimisation of Multiple Time-Step Hybrid Monte Carlo Wang–Landau Simulations in the Isobaric–Isothermal Ensemble for the Determination of Phase Equilibria. *Mol. Simul.* **2010**, *36*, 544–551.
- (55) Desgranges, C.; Hicks, J. M.; Magness, A.; Delhommelle, J. Phase Equilibria of Polyaromatic Hydrocarbons by Hybrid Monte Carlo Wang–Landau Simulations. *Mol. Phys.* **2010**, *108*, 151–158.
- (56) Ngale, K. N.; Desgranges, C.; Delhommelle, J. Wang–Landau Configurational Bias Monte Carlo Simulations: Vapour–Liquid Equilibria of Alkenes. *Mol. Simul.* **2012**, *38*, 653–658.
- (57) Desgranges, C.; Ngale, K.; Delhommelle, J. Prediction of Critical Properties for Naphthalene, Triphenylene and Chrysene by Wang–Landau Simulations. *Fluid Phase Equilib.* **2012**, *322–323*, 92–96.
- (58) Aleksandrov, T.; Desgranges, C.; Delhommelle, J. Numerical Estimate for Boiling Points via Wang–Landau Simulations. *Mol. Simul.* **2012**, *38*, 1265–1270.
- (59) Escobedo, F.; de Pablo, J. J. Expanded Grand Canonical and Gibbs Ensemble Monte Carlo Simulation of Polymers. *J. Chem. Phys.* **1996**, *105*, 4391.
- (60) Lyubartsev, A. P.; Martsinovski, A. A.; Shevkunov, S. V.; Vorontsov-Velyaminov, P. N. New Approach to Monte Carlo Calculation of the Free Energy: Method of Expanded Ensembles. *J. Chem. Phys.* **1992**, *96*, 1776–1783.
- (61) Muller, M.; Paul, W. Measuring the Chemical Potential of Polymer Solutions and Melts in Computer Simulations. *J. Chem. Phys.* **1994**, *100*, 719–724.
- (62) Shi, W.; Maginn, E. J. Continuous Fractional Component Monte Carlo: An Adaptive Biasing Method for Open System Atomistic Simulations. *J. Chem. Theory Comp.* **2007**, *3*, 1451–1463.
- (63) Singh, J. K.; Errington, J. R. Calculation of Phase Coexistence Properties and Surface Tensions of *n*-Alkanes with Grand-Canonical Transition-Matrix Monte Carlo Simulation and Finite-Size Scaling. *J. Phys. Chem. B* **2006**, *110*, 1369–1376.
- (64) Escobedo, F. A.; Martinez-Veracoechea, F. J. Optimized Expanded Ensembles for Simulations involving Molecular Insertions and Deletions. I. Closed Systems. *J. Chem. Phys.* **2007**, *127*, 174103.
- (65) Escobedo, F. A.; Martinez-Veracoechea, F. J. Optimization of Expanded Ensemble Methods. *J. Chem. Phys.* **2008**, *129*, 154107.
- (66) Rane, K. S.; Murali, S.; Errington, J. R. Monte Carlo Simulation Methods for Computing Liquid–Vapor Saturation Properties of Model Systems. *J. Chem. Theory Comput.* **2013**, *9*, 2552–2566.
- (67) Rane, K. S.; Errington, J. R. Using Monte Carlo Simulation to Compute Liquid–Vapor Saturation Properties of Ionic Liquids. *J. Phys. Chem. B* **2013**, *117*, 8018–8030.
- (68) Koenig, A. R. V.; Desgranges, C.; Delhommelle, J. Adsorption of Hydrogen in Covalent Organic Frameworks using Expanded Wang–Landau Simulations. *Mol. Simul.* **2014**, *40*, 71–79.
- (69) Hicks, E. A.; Desgranges, C.; Delhommelle, J. Adsorption and Diffusion of the Antiparkinsonian Drug Amantadine in Carbon Nanotubes. *Mol. Simul.* **2014**, *40*, 656–663.
- (70) Allen, M. P.; Tildesley, D. J. *Computer Simulation of Liquids*; Clarendon Press: Oxford, 1987.
- (71) Vargaftik, N. B.; Vinogradov, Y. K.; Yargin, V. S. *Handbook of Physical Properties of Liquids and Gases*; Begell House: New York, 1996.
- (72) Huber, M. L.; Laesecke, A.; Friend, D. G. Correlation for the Vapor Pressure of Mercury. *Ind. Eng. Chem. Res.* **2006**, *45*, 7351–7361.
- (73) Hong, X.; Inui, M.; Matsusaka, T.; Ishikawa, D.; Huq Kazi, M.; Tamura, K. X-ray Diffraction Measurements for Expanded Fluid Mercury Using Synchrotron Radiation: from the Liquid to Dense Vapor. *J. Non-Cryst. Solids* **2002**, *312*, 284–289.
- (74) Maruyama, K.; Endo, H.; Hoshino, H.; Hensel, F. Void Structure and Intermediate-Range Fluctuations in the Metal–Non-metal Transition Range in Expanded Liquid Hg. *Phys. Rev. B* **2009**, *80*, 014201.
- (75) Ruland, W.; Hensel, F. Critical Region and Metal–Nonmetal Transition in Expanded Fluid Mercury: Advanced Evaluation of Small-Angle X-ray Scattering Data. *J. Appl. Crystallogr.* **2010**, *43*, 244–249.